Published in final edited form as:
Nat Neurosci. 2014 February ; 17(2): 304–311. doi:10.1038/nn.3606.

Molecular drivers and cortical spread of lateral entorhinal cortex dysfunction in preclinical Alzheimer's disease

Usman A Khan[1,2,3], **Li Liu**[1,4], **Frank A Provenzano**[1,2], **Diego E Berman**[1,4], **Caterina P Profaci**[1,4], **Richard Sloan**[5], **Richard Mayeux**[1,2], **Karen E Duff**[1,4], and **Scott A Small**[1,2,6]

[1]Taub Institute for Research on Alzheimer's Disease and the Aging Brain, Columbia University College of Physicians and Surgeons, New York, New York, USA

[2]Department of Neurology, Columbia University College of Physicians and Surgeons, New York, New York, USA

[3]Program in Neural and Behavioral Science, State University of New York Downstate Medical Center, Brooklyn, New York, USA

[4]Department of Pathology, Columbia University College of Physicians and Surgeons, New York, New York, USA

[5]Department of Psychiatry, Columbia University College of Physicians and Surgeons, New York, New York, USA

[6]Department of Radiology, Columbia University College of Physicians and Surgeons, New York, New York, USA

Abstract

The entorhinal cortex has been implicated in the early stages of Alzheimer's disease, which is characterized by changes in the tau protein and in the cleaved fragments of the amyloid precursor protein (APP). We used a high-resolution functional magnetic resonance imaging (fMRI) variant that can map metabolic defects in patients and mouse models to address basic questions about entorhinal cortex pathophysiology. The entorhinal cortex is divided into functionally distinct regions, the medial entorhinal cortex (MEC) and the lateral entorhinal cortex (LEC), and we exploited the high-resolution capabilities of the fMRI variant to ask whether either of them was affected in patients with preclinical Alzheimer's disease. Next, we imaged three mouse models of

Correspondence should be addressed to K.D. (ked2115@columbia.edu) or S.A.S. (sas68@columbia.edu).

Accession codes. The microarray data were submitted to the Gene Expression Omnibus database with series accession number GSE49311.

Any Supplementary Information and Source Data files are available in the online version of the paper.

AUTHOR CONTRIBUTIONS

U.A.K. performed the mouse and human fMRI analysis and wrote the manuscript. L.L. helped with mouse breeding and performed the histological analyses in mice models. F.A.P. performed the human fMRI post-processing. D.E.B. performed the microarray and other molecular analyses. C.P.P. helped with the histological analyses and mouse breeding. R.S. recruited the young human subjects. R.M. recruited and characterized the older human subjects. K.E.D. supervised the generation and histological analyses in the mouse models and wrote the manuscript. S.A.S. designed the studies, helped with the statistical analyses and wrote the manuscript.

COMPETING FINANCIAL INTERESTS

The authors declare no competing financial interests.

disease to clarify how tau and APP relate to entorhinal cortex dysfunction and to determine whether the entorhinal cortex can act as a source of dysfunction observed in other cortical areas. We found that the LEC was affected in preclinical disease, that LEC dysfunction could spread to the parietal cortex during preclinical disease and that APP expression potentiated tau toxicity in driving LEC dysfunction, thereby helping to explain regional vulnerability in the disease.

A convergence of histological[1,2] and imaging[3,4] studies has implicated the entorhinal cortex as a primary site of dysfunction in Alzheimer's disease. At a molecular level, Alzheimer's disease is characterized by changes in the tau protein and an accumulation of cleaved products of APP. Studies have shown that dysfunction in the entorhinal cortex is associated with both tau and amyloid abnormalities[5–7]. A parallel series of studies have shown that the entorhinal cortex consists of two very distinct subdivisions, the MEC and LEC. Each division houses a population of neurons distinct in their circuit connections within the medial temporal lobe (MTL), in their cognitive roles, in their morphological features and in their physiological properties[8–11]. Accordingly, guided by the general principle of regional vulnerability, we hypothesized that Alzheimer's disease differentially targets one subdivision over the other.

Alzheimer's disease is a chronically progressive disorder that causes synaptic and metabolic dysfunction before cell death[12] and that begins in a 'preclinical' stage before progressing to mild cognitive impairment and, ultimately, dementia[13]. To test the hypothesis of differential dysfunction in the entorhinal cortex, it is important to use a high-resolution functional imaging variant that can reliably visualize the LEC and MEC and to apply this tool in the earliest preclinical stages of Alzheimer's disease.

Of functional imaging techniques sensitive to metabolism, cerebral blood volume (CBV) generated with an exogenous contrast agent and mapped with MRI[14] has the highest spatial resolution. As a functional imaging measure, CBV has proven to be tightly coupled to regional metabolism in healthy and diseased brains[15,16], including in Alzheimer's disease[17]. Advantageous for visualizing small regions of the human brain, the high resolution of CBV-fMRI is particularly useful in cross-species imaging studies, where the goal is to compare dysfunction in patients and animal models using the same imaging readout. Indeed, previous studies have used CBV-fMRI in patients and animal models to localize metabolic dysfunction in Alzheimer's disease[4] and cognitive aging[4,18]. Those studies, however, relied on manual labeling of regions of interest (ROIs). Thus, although CBV-fMRI has sufficient spatial resolution to dissociate the MEC from the LEC in principle, manual labeling cannot distinguish these divisions without reliable anatomical landmarks. To overcome this limitation, we recently incorporated and optimized newly developed processing techniques that allow for automated ROI and voxel-based analysis of CBV images in humans and mouse models. In our first series of human studies, we applied these tools to analyze CBV maps of patients with preclinical Alzheimer's disease, finding that dysfunction localizes to the LEC and is linked to dysfunction in other cortical regions, such as the precuneus in the parietal lobe.

Although studies have suggested that entorhinal cortex dysfunction in Alzheimer's disease is associated with both tau and amyloid abnormalities, it is unknown how these abnormalities

interact in driving dysfunction, particularly during preclinical stages. We addressed this and other questions in mice. Using the neuropsin promoter system to preferentially express disease-causing mutations in tau or APP in the entorhinal cortex (similar to published mice[19–21]), we crossed these mice to generate a mouse model that expresses both human tau (*MAPT*) and APP (*APP*) mutations in the entorhinal cortex. Although there was some expression of human tau and APP outside of the entorhinal cortex as a result of leaky expression of the responder transgenes, the system allowed for a very high level of expression in the entorhinal cortex relative to other regions. We imaged over 200 mice in two age groups and found that the LEC was particularly sensitive to tau and amyloid expression, that the accumulation of APP products acted to potentiate and accelerate tau toxicity, and that dysfunction in the LEC could spread to the parietal cortex.

RESULTS

Entorhinal cortex dysfunction and its cortical links

We used CBV-fMRI to image 96 adults who were free of dementia or mild cognitive impairment at baseline and who were prospectively followed for an average of 3.5 years. At follow-up, 12 individuals were found to have progressed to mild Alzheimer's disease dementia and were assigned the diagnosis of preclinical Alzheimer's disease at baseline. The 84 individuals who remained free of dementia or mild cognitive impairment were used as a control group for comparison (Table 1). A small, but significant, difference in age was found in the preclinical group (mean age of 82 years for the preclinical group and 78 years for the control group; $t = 5.4$, $P = 0.02$), but there was no difference in sex distribution.

As previously described[4], we used gadolinium-enhanced T1-weighted scans (acquired perpendicular to the hippocampal long axis; in-plane resolution = 0.78 × 0.78 mm, slice thickness = 3 mm) to derive steady-state CBV maps. To perform automated whole-brain ROI analysis, we first determined whether FreeSurfer technology could successfully segment individual CBV maps (Fig. 1a). As no laterality was hypothesized, we averaged left and right regions to reduce multiple testing. An ANOVA was used to compare regional CBV between the preclinical Alzheimer's disease and control groups, with age included as a covariate. Analysis was performed in two steps. First, we focused on regions in the MTL. Compared with the control group, the preclinical group had significant CBV reductions in the entorhinal cortex ($F_{1,95} = 4.6$, $P = 0.03$) and parahippocampal gyrus ($F_{1,95} = 4.7$, $P = 0.03$) (Fig. 1b), but not in the hippocampus proper ($F_{1,95} = 1.9$, $P = 0.2$). Second, we included other brain regions, finding significant CBV reductions in the lingual cortex ($F_{1,95} = 4.9$, $P = 0.03$), the frontal pole ($F_{1,95} = 4.6$, $P = 0.04$) and the anterior cingulate ($F_{1,95} = 6.5$, $P = 0.01$), and trends in the precuneus ($F_{1,95} = 3.7$, $P = 0.059$) and cuneus ($F_{1,95} = 3.9$, $P = 0.052$). Finally, we carried out a correlation analysis in the preclinical group between CBV values in the entorhinal cortex and other identified hypometabolic regions. After correcting for multiple testing, a significant correlation was observed only with the parahippocampal gyrus (Pearson correlation = 0.83, $P = 0.002$) and precuneus (Pearson correlation = 0.75, $P = 0.005$), suggesting a selective link between the entorhinal cortex dysfunction and dysfunction in these interconnected cortical regions (Fig. 1c).

LEC versus MEC dysfunction

The entorhinal cortex ROI did not distinguish the MEC from the LEC, whereas the parahippocampal gyrus ROI did distinguish the parahippocampal cortex from the perirhinal cortex (PRC), which are important divisions of the MTL organized into functionally distinct circuits[11]. To pinpoint the precise sites of dysfunction, we co-registered CBV maps using an asymmetric diffeomorphic approach[22] and performed a voxel-based analysis in the temporal lobes. A factorial analysis was carried out, including age and sex as covariates, and we found that, compared with the controls, the preclinical group had reduced CBV specifically in the LEC, the transentorhinal cortex and the PRC (Fig. 2a,b).

Delayed retention is a cognitive operation that has been associated with the entorhinal cortex[23] and is sensitive to the earliest stages of disease[24]. We therefore performed a regression analysis between MTL CBV and performance on a delayed retention task[23], covarying for age and sex. A selective correlation was found in the LEC (Fig. 2c).

Drivers of LEC dysfunction and its cortical spread

Using the neuropsin promoter system[25], we generated three colonies of mice that expressed a pathological human tau transgene (*Opn5-tTA; tTA-MAPT*, or EC-Tau), a pathological human APP transgene (*Opn5-tTA; tTA-APP*, or EC-APP), or both APP and tau transgenes (*Opn5-tTA; tTA-APP; tTA-MAPT*, EC-APP/Tau). Across all colonies, a total of 127 mice were generated that were younger than 6 months of age, and all of them were imaged with CBV-fMRI as previously described[26]. Voxel-based analyses were performed in each colony to map patterns of dysfunction. We found that, in the EC-APP and EC-Tau colonies, there were no detectable CBV differences between the non-expressing genotypes and their wild-type littermates. For subsequent analyses, we used these non-expressing genotypes and wild-type littermates as controls.

A three-dimensional volume of the mouse brain was rendered (3DSlicer software package) using a postmortem anatomical template[27] to determine the location of MTL regions (Fig. 3a). Voxel-based analysis of the fMRI data revealed that, in the EC-Tau colony, mice expressing tau ($N = 11$, mean age = 3.6 months) showed no detectable CBV effects compared with their controls ($N = 15$, mean age = 4.2 months) (Fig. 3b). In the EC-APP colony, mice expressing APP ($N = 23$, mean age = 3.4 months) showed CBV reductions in the MEC and CA1 compared with their controls ($N = 33$, mean age = 3.6 months) (Fig. 3b). In the EC-APP/Tau colony, mice expressing both APP and tau ($N = 22$, mean age = 3.2) showed CBV reductions in the LEC compared with mice in the colony expressing just APP or tau, or other controls ($N = 23$, mean age = 3.3 months) (Fig. 3b,c).

In the mice co-expressing APP and tau, CBV reductions were also found in the PRC, transentorhinal cortex and the posterior parietal cortex (PPC) (Fig. 3d). As we observed in rendered three-dimensional volumes of the mouse and human brains, the CBV reductions in the mouse PRC and PPC were regions that are homologous to the humans found linked to the entorhinal cortex dysfunction (Fig. 4), with the notable difference that the dominant effects in the mice were observed in the left hemisphere.

APP potentiates tau toxicity in the LEC

To test for age-dependent changes, we imaged an additional 103 mice older than 6 months of age (6–12 months of age) and mapped age-by-genotype interactions in each colony. In the EC-Tau colony, older mice expressing tau ($N = 9$, mean age = 8.8 months) showed an age-dependent CBV worsening in the LEC compared with their controls ($N = 24$, mean age = 8.8 months) (Fig. 5a). In the EC-APP colony, older mice expressing APP ($N = 18$, mean age = 7.4 months) showed an age-dependent CBV worsening in the MEC compared with their controls ($N = 21$, mean age = 7.2 months) (Fig. 5a). In the EC-APP/Tau colony, older mice co-expressing APP and tau ($N = 11$, mean age = 12.1 months) showed an age-dependent CBV worsening in the LEC, PRC and PPC compared with mice expressing APP or tau alone ($N = 20$, mean age = 11.6 months) (Fig. 5b). These results suggest that tau alone, but not APP alone, can ultimately cause LEC dysfunction, and that APP expression acts to accelerate and potentiate tau toxicity in driving LEC dysfunction and the observed spread to the PRC and PPC (Fig. 5a,b).

Histological markers of tau and APP expression

We carried out a detailed histological analysis in both the younger mice (mean age = 4 months; EC-APP/Tau, $n = 11$; EC-APP, $n = 10$; EC-Tau, $n = 6$) and older mice (mean age = 12 months; EC-APP/Tau, $n = 7$; EC-APP, $n = 5$; EC-Tau, $n = 5$). We used the 6E10 antibody to map human APP and the processed fragments β-CTF and Aβ (hereafter referred to as APP/Aβ), CP27 to map human tau, and an MC1 antibody to map human tau in an abnormal conformation that is seen in the brains of individuals with Alzheimer's disease[28]. In younger mice, human APP/Aβ was observed throughout the entorhinal cortex of EC-APP and EC-APP/Tau mice; however, consistent with the expression pattern of *Opn5-tTA*[25], a higher level of APP/Aβ was observed in the MEC versus the LEC (Fig. 6a). As previously reported[21], a few Aβ plaques were seen in the MEC and APP/Aβ staining was also detected in the hippocampus proper. No differences in APP/Aβ accumulation were observed between the EC-APP and EC-APP/Tau mice. As with APP, a similar pattern of entorhinal cortex expression was observed for human tau in younger EC-Tau and EC-APP/Tau mice. As detected by CP27, human tau was observed throughout the entorhinal cortex, but was most abundant in the MEC (Fig. 6a). A similar pattern was observed for abnormal tau, as detected with the MC1 antibody (Fig. 6a). As previously reported[19], tau staining was also detected in regions of the hippocampus proper that project from the entorhinal cortex.

In older mice, APP/Aβ and amyloid deposits were detected throughout the entorhinal cortex in both EC-APP and EC-APP/Tau mice (Fig. 6b). No APP-related differences were observed between the EC-APP and EC-APP/Tau mice. Distinct abnormalities were detected, however, in the older EC-APP/Tau mice when tau was mapped and characterized. Compared with younger EC-APP/Tau mice or older EC-Tau mice, older EC-APP/Tau mice showed more intense somatodendritic MC1 staining in many entorhinal cortex neurons (Fig. 6b). There appeared to be less neuropil staining, which indicates a relocalization of tau from axons into the somatodendritic compartments (Fig. 6c). A similar staining pattern for tau was also detected by CP27, an antibody that specifically detects human tau independent of conformation and phosphorylation status (Fig. 6b). Compared with the older EC-Tau mice, a semiquantitative analysis revealed a reliable increase in MC1-positive neuronal cell bodies

in the entorhinal cortex in the older EC-APP/Tau mice, mainly in the MEC (Fig. 6c). To further characterize this effect, we performed additional staining using the AT8 antibody, which recognizes tau phosphorylated at S202/T205 (both human and murine). Compared with older EC-Tau mice, older EC-APP/Tau mice showed more intense somatodendritic AT8 immunoreactivity (Fig. 6c).

Examining the parietal lobe revealed amyloid deposits, including in the PPC, in both older EC-APP and EC-APP/Tau mice (Fig. 6d). As in the younger mice, no clear APP-related differences were observed between the EC-APP and EC-APP/Tau mice. In the parietal lobe, we did not detect clear evidence of somatodendritic MC1 staining (Fig. 6d) in either the EC-Tau or EC-APP/Tau mice, or enhanced somatodendritic staining of AT8 in EC-APP/Tau versus EC-Tau mice (Fig. 6d). Although there was no evidence for somatodendritic staining, MC1-positive dystrophic neurites were detected in the parietal lobe of some of the EC-APP/Tau mice, which colocalized with amyloid deposits (data not shown). The source of this human tau is unknown and it could represent human tau originating in entorhinal cortex neurons or a low level of human tau expressed in the cortex of rTg4510 mice as a result of a slight leakiness of the responder transgene.

Evidence that high metabolism tracks regional vulnerability

As noted in the mouse studies, the left LEC was affected more than the right. To identify factors that might account for this regional pattern of vulnerability, we examined the mice for molecular or imaging factors that anatomically localized to the left versus the right entorhinal cortex. By examining histological markers, we excluded the possibility that there was overtly higher APP or tau expression in the left versus right entorhinal cortex of control mice (data not shown). By examining CBV images in individual cases, we excluded the possibility that signal quality varies in the left versus the right entorhinal cortex, consistent with previous studies using this approach. Generating gene-expression profiles from the left and right entorhinal cortex in younger wild-type mice revealed left and right differences, but none that provide a clear reason for differential vulnerability.

In considering other reasons for the regionally selective effects, we were intrigued by a previous postmortem study that suggested that the LEC might have very high basal metabolism[29–31]. Accordingly, we generated ROIs of LEC and MEC and applied them to 52 control mice from the neuropsin data set (Fig. 7a). We performed a repeated-measures ANOVA, including two within-subject factors, entorhinal cortex region (MEC versus LEC) and laterality (left versus right), and found a significant region-by-laterality interaction ($F_{1,51} = 8.376$, $P = 0.006$; Fig. 7b) and significant main effects of region ($F_{1,51} = 678.959$, $P < 0.001$) and laterality ($F_{1,51} = 9.148$, $P = 0.004$). Simple comparisons revealed that the interaction and main effect of laterality were driven by the left LEC having the highest CBV among regions (univariate ANOVA: $F_{1,52} = 164.114$, $P < 0.001$), particularly compared against the right LEC (paired $t_{51} = 3.067$, $P = 0.003$) (Fig. 7c). This observation, suggesting higher metabolism in the left LEC of young wild-type mice, anatomically corresponded to the pattern of dysfunction observed in transgenic mice,

Higher basal metabolism in unaffected individuals might confer vulnerability. If so, and based on the pattern of entorhinal cortex vulnerability observed in humans, we hypothesized

that the LEC should have higher CBV in healthy humans. Because of the difficulty in excluding incipient disease in even cognitively normal older subjects, we imaged an additional 35 young healthy humans subjects (mean age = 29 years) and measured CBV from ROIs of the LEC and MEC (Fig. 7a). A repeated-measures ANOVA was performed, including two within-factor factors, region (MEC versus LEC) and laterality (left versus right). We did not detect a laterality effect, but, as hypothesized and similar to young wild-type mice, we found significantly higher CBV in the LEC than in the MEC ($F_{1,34}$ = 1,056.155, $P < 0.001$); in fact, the LEC CBV was higher than that of the other cortical regions examined (Fig. 7c).

DICUSSION

We began with observations in patients with preclinical Alzheimer's disease and then turned to mouse models to clarify human findings in an experimental setting. Although the protocol for acquiring CBV images was identical to that used in our previous studies, we introduced a number of new processing techniques with which the imaging data was analyzed. We found that FreeSurfer technology can be applied directly to CBV images to generate automated whole-brain ROIs, bypassing the need to interpolate functional-to-structural images and thereby preserving anatomical fidelity. Our ROI analysis revealed that, in the MTL, entorhinal cortex and parahippocampal gyrus were affected in preclinical Alzheimer's disease, and the hippocampus proper was relatively preserved. In addition, entorhinal cortex dysfunction was linked to dysfunction in the parahippocampal gyrus and the precuneus cortex in the parietal lobe.

Although the whole-brain analysis identified dysfunction in the entorhinal cortex, the ROI encompassed the entire entorhinal cortex containing both the LEC and MEC. A voxel-based analysis was required to answer a key question motivating our study. Refining the ROI-based findings, the voxel-based analysis revealed that, in the entorhinal cortex, it was the LEC that was primarily affected in preclinical Alzheimer's disease. More broadly, we found that the transentorhinal cortex and PRC were also affected (Fig. 2a,b). Further confirming the ROI analysis, other subregions of the hippocampal circuit were unaffected in preclinical disease.

There has been a growing interest in understanding the distinct cognitive roles of the entorhinal cortex divisions, and our voxel-based analysis revealed that performance on delayed retention of hippocampal-dependent tasks correlates selectively with LEC CBV (Fig. 2c). Previous human fMRI studies have shown that the entorhinal cortex is involved in retaining hippocampal-dependent memories over brief delays[23,32,33], although these studies could not dissociate the MEC from the LEC. Recording studies in non-human primate and rodent[10,34,35] have shown that it is specifically neurons in the LEC that have distinct electrophysiological properties that support a role in delayed retention. Our high-resolution fMRI results confirmed this LEC-selective role in human subjects. As delayed retention is affected in preclinical Alzheimer's disease decades before the onset of dementia[24] and is relatively unaffected by aging[36,37], our results identify an anatomical locus for the cognitive phenotype of early disease. The MEC and LEC are each parts of different pathways in the MTL. Whereas the MEC interconnects with the parahippocampal cortex to form the

posterior pathway, the LEC interconnects with the PRC to form the anterior pathway[11]. By selectively implicating the LEC and perirhinal cortex, our results suggest that the anterior pathway is differentially vulnerable to the early stages of disease.

We generated three colonies of genetically engineered mice to clarify our observations in human patients. The first two expressed either abnormal tau or APP predominately in the entorhinal cortex. However, as the entorhinal cortex in Alzheimer's disease is associated with both tau- and APP-related abnormalities[5–7], we developed a third mouse model that expresses both abnormal tau and APP in the entorhinal cortex. We found that the LEC in young mice was affected only when tau and APP were co-expressed (Fig. 3b–d). Because the neuropsin promoter expresses genes preferentially in the MEC over the LEC, the observed dysfunction in the LEC was not driven simply by a dose effect of two genes. Rather, our results suggest that this division of the entorhinal cortex is particularly sensitive to the molecular sequelae of tau and APP expression.

To gain a mechanistic understanding of how tau and APP expression interact in driving LEC dysfunction, we imaged mice at older ages. In addition to observing an age-dependent worsening of LEC dysfunction in the mice expressing both tau and APP, we found that the LEC became affected in older mice expressing tau alone, but not in older mice expressing APP alone. Consistent with previous studies[38], it appears that, at older ages and with sufficient levels of pathology, tau alone can ultimately affect the LEC. Even at later time points, however, the coexpression of tau and APP caused worsening LEC dysfunction compared with tau alone. We can conclude that APP expression acts to potentiate and accelerate tau toxicity in driving LEC dysfunction.

Mice expressing both tau and APP were found to have dysfunction in areas in which transgene expression was not expected, the PRC and PPC, and dysfunction in these regions worsened with age. These regions are similar to the cortical regions that we found to be linked to entorhinal cortex dysfunction in humans, supporting the interpretation that the LEC is an anatomical source from which disease can then spread. Previous studies have documented that the entorhinal cortex can act as an anatomical source for Alzheimer's disease–related spread via two mechanisms. The first is 'functional' spread and was best demonstrated in a study that administered selective lesions to the entorhinal cortex and PRC of nonhuman primates[39]. Using functional imaging, these selective lesions were found to cause hypometabolism in distal cortical sites, including regions in the posterior parietal lobe[39]. A disconnection mechanism has been proposed to account for functional spread in which primary dysfunction in the entorhinal cortex results in secondary dysfunction in regions connected to the entorhinal cortex. The second mechanism is trans-synaptic spread, which was shown by expressing either APP or tau in the entorhinal cortex of mice, and observing changes in distal sites connected to the entorhinal cortex[19–21]. We did not observe clear evidence of worsening histological changes in distal regions of the mice expressing tau and APP; thus, our results are more consistent with the idea of functional spread. However, given that histological changes might elude detection, we cannot rule out the possibility of trans-synaptic spread. Indeed, plaques and dystrophic neurites were detected in the parietal lobe of older EC-APP/Tau mice, but there was no difference in general to EC-APP littermates. In either scenario of cortical spread, PPC hypometabolism is reliably observed in

Alzheimer's disease, so much so that when observed with functional imaging it is often considered diagnostic. Our results suggest that, during early stages of disease, PPC hypometabolism can reflect primary pathology in the LEC.

Our histological analysis replicated previous transgenic studies[27] showing that pathological APP expression acts to accelerate tau-related histological changes, a relationship similar to that observed for image-detected dysfunction. As we observed in the entorhinal cortex, the anatomical distribution of histological markers used to map human APP and its fragments or tau did not simply overlap with the anatomical pattern of imaging-detected dysfunction. This observation is reminiscent of human imaging studies showing imperfect concordance between the anatomical distribution of amyloid plaques and regional hypometabolism[40]. Our results highlight the ongoing debate over which precise molecular 'species' derived from tau or APP (that is, which fragment, conformation or oligomer) acts as the dominant neurotoxin. Resolving this issue is beyond the scope of the current study, but our results suggest that some fragment of APP acts to potentiate a toxic species of tau.

In young unaffected mice and human subjects, we found evidence for high metabolism in the LEC that tracked the anatomical pattern of vulnerability. Postmortem studies have documented clusters of extremely high metabolism in superficial layers of the entorhinal cortex[29,30] and our fMRI results confirm one observation that would predict that the highest metabolism would be present in the LEC[41]. Basal metabolism typically reflects the activity and morphological organization of a region's dendritic arbor, which is unique in the LEC[8], and can influence the processing or sensitivity to tau and APP processing. Not only does activity affect the manner in which APP is processed in dendrites[42], but tau itself has been found to be important for dendritic function[43] and structure[44]. Early on and throughout life, an unusual accumulation of tau is observed in the dendrites and soma of the LEC[1], yet, consistent with our mouse studies, there is no evidence that an early accumulation of dendritic tau in the LEC is neurotoxic. It is possible that the accumulation of somatodendritic tau relates to the LEC's distinct dendritic characteristics and needs, but it is notable that dendritic tau has been shown to mediate APP-related neurotoxicity[43]. Informed by our imaging findings, we propose that the unique dendritic arbor in superficial layers of the LEC renders it vulnerable, and when an accelerated accumulation of APP fragments occurs with disease onset, the LEC is affected first and foremost and dysfunction can then spread cortically.

ONLINE METHODS

Human subjects

Participants for the primary human study were identified from a community-based fMRI study of individuals 65 years and older[45], who received a detailed neuropsychological and neurological evaluation[46] and who were free of Alzheimer's disease dementia[47], mild Alzheimer's disease[48] or mild cognitive impairment indicative of the pre-dementia stage of the disease in this population[49]. Table 1 summarizes baseline and changes in cognition for the group that progressed to dementia at follow-up (progressors) and those who did not progress (non-progressors) in the following domains: memory was evaluated using the Selective Reminding Test, language was evaluated using the summary Benton Naming Test,

visuospatial ability was evaluated using the Rosen Drawing Task, and abstract reasoning was evaluated using the Wechsler Adult Intelligence Scale–Revised similarities. An ANOVA was used to compare between group differences in baseline scores or change scores, covarying for age and sex.

Transgenic mice

Two tTA inducible responder mouse lines expressing either mutant human APP or tau transgenes were crossed with the neuropsin-tTA line to generate three colonies of entorhinal cortex predominant expressing mice. The inducible tau line (rTg4510) expressing human, four-repeat tau with the P301L mutation (4R0N tauP301L)[50] was used to generate the EC-Tau colony. The inducible APP line encodes a mutant, chimeric mo/huAPP695 (swe/ind KM670, 671NL and V717F) transgene[51] and was used to generate the EC-APP colony. The EC-APP/Tau colony was generated by crossing the two mouse lines, the EC-APP and EC-Tau mice, and the resulting line was hemizygous at each locus.

Image acquisition

As previously described[52], for the primary human study, images were acquired with a 1.5-T Philips Intera scanner, generating T1-weighted images (time to repeat, 20 ms; time to echo, 6 ms; flip angle, 25 degrees; in plane resolution, 0.78 mm × 0.78 mm; slice thickness, 3 mm) acquired perpendicular to the long axis of the hippocampus before and 4 min after intravenous administration of the contrast agent gadolinium (0.1 mmol kg^{-1}). For the secondary study in young subjects, T1-weighted images (repetition time, 20 ms; echo time, 6 ms; flip angle, 25 degrees; in plane resolution, 0.68 mm; slice thickness, 3 mm) were acquired at 3 T using a Philips Integra 3T magnet.

In mice, images were acquired with a Bruker AVANCE 400WB spectrometer outfitted with an 89-mm bore, 9.4-T vertical Bruker magnet (Oxford Instruments), a 30-mm inner-diameter birdcage radio frequency coil, and a shielded gradient system (100 G cm^{-1}) before and 37.5 min after intraperitoneal injections of the contrast agent gadolinium[52] (10 mmol kg^{-1}). Mice were anesthetized using a gaseous mixture of 30% O_2, 70% N_2 and isoflurane (3% volume for induction, 1.1–1.5% for maintenance at 1 l min^{-1} air flow, via a nose cone). T2-weighted images were acquired with a fast-spin echo acquisition (time to repeat, 2,000 ms; time to echo, 70 ms; rapid acquisition and relaxation enhancement factor, 16; in plane resolution, 86 μm; slice thickness, 500 μm).

Generating CBV maps

For human scans, pre-contrast images were subtracted from post-contrast images to generate a raw subtracted volume. Intra-subject and intra-modal co-registrations used a symmetric rigid body alignment incorporating a robust statistics measure[53]. Raw image values were normalized to the mean signal intensity of the subject's superior sagittal sinus. The superior sagittal sinus was isolated in each post-contrast image using a modified Frangi vesselness[54] filter and pre-defined ROI. This filter uses three-dimensional eigenvalues of the Hessian of the image to calculate global shape parameters of the superior sagittal sinus ROI, including, but not limited to, its anisotropic features. The isolated image was then eroded using a standard kernel to ensure the ROI sits entirely in the sinus cavity. The mask was applied to

the subtracted image, and the measure of absolute blood was calculated as the mean of that image. To rule out the effects of large vessels, two methods of vessel filtering were used: fitting a bimodal Gaussian to the histogram of data and performing an expectation-maximization segmentation. The union of the aforementioned methods was used to make a binary mask, which was then applied to the generated CBV image. As previously described[4,52], CBV was mapped according to changes in the transverse relaxation time (ΔR_2) induced by gadolinium injection. CBV was derived by normalizing ΔR_2 to the mean ΔR_2 signal present in the internal jugular vein, as delineated by a blinded rater.

ROI analysis

Human scans were first processed through the FreeSurfer 5.1 pipeline to semi-automatically segment cortical and subcortical features of the whole brain[55]. Briefly, the pre-contrast T1-weighted image, acquired for CBV mapping, was intensity-normalized and bias-field corrected, and was then skull-stripped and used to construct a smoothed surface-based tessellation of cortical surface. Each subject's surface was mapped to a spherical atlas and assigned a cortical surface label based on its surface curvature profile. In addition, a Euclidian mapping framework was used to align and segment subcortical features.

Voxel-based analysis

Voxel-based analyses in humans were performed separately on the left and right temporal lobes by combining the following FreeSurfer generated segmentations: superior temporal gyrus, middle temporal gyrus, inferior temporal gyrus, temporal pole, fusiform gyrus, entorhinal cortex, amygdala, inferior horn of the lateral ventricle, hippocampus, inferior horn choroid plexus, transverse temporal gyrus, parahippocampal gyrus, the isthmus and cingulate gyri, lingual gyrus, as well as an unknown label. These were then further delimited to a 'temporal lobe proper' using the superior temporal gyrus, parahippocampal cortex, transverse temporal gyrus, fusiform gyrus and inferior temporal gyrus as boundaries. In mice, images were bias-field corrected[56] and manually skull stripped to yield whole-brain volumes.

For both humans and mice, image processing was conducted using custom bash and Matlab scripts. Volumes were co-registered into a group-wise template space using an inverse-inconsistent diffeomorphic co-registration algorithm, as described previously[22]. Briefly, the co-registration instantiates a stationary vector field that smoothly warps images in their native coordinate space while conserving topology. Furthermore, each iteration of the co-registration was optimized by a Jacobian weighting term that encodes local distortions generated by the warp. This method yields robust and accurate alignment of images within their native coordinate space. The co-registration consisted of three steps. Anatomical images were first aligned to a randomly selected image in their data set using a linear transformation with 12 degrees of freedom. Next, the linearly aligned images were used to determine the optimal diffeomorphic transformation necessary to warp each image in the data set to an unbiased template image. Each iteration of the pairwise diffeomorphic registration between each image and the template generated a normalized warp with an average deformation of zero, ensuring that the template image generated was not biased by

relative local volume loss or expansion between groups. Finally, the linear transformation and nonlinear warps were applied to corresponding CBV maps for each subject.

CBV maps were analyzed using a general linear model implemented in SPM8 (Wellcome Department of Imaging Neuroscience). Data were modeled in a factorial framework with genotype and time point included as the between-subjects factors, and sex as a covariate. Individual genotypes were contrasted using Student's *t* test, and the genotype-time interaction effect was contrasted with an *F* test. In humans, a general linear model was also used to regress delayed-retention task score against CBV, and contrasted with Student's *t* test. Results were corrected for multiple comparisons using a family-wise error rate of $P < 0.05$, and thresholded to include only those clusters with an extent greater than 30 voxels. Thresholded *t* maps from individual group comparisons were then overlaid onto their respective groupwise templates in cross-section using 3DSlicer (http://www.slicer.org), and also displayed as maximum intensity projections over mesh models of the groupwise template.

LEC versus MEC analysis

Using the co-registration technique described above, structural images from 47 young (<6 months) control mice (C57 13, neuropsin 16, tetO-APP 13, tetO-tau 5) and 35 young human subjects (age = 23–39, mean age = 29.3 years, 18 males and 17 females) were used to generate control-only mouse and human group-wise image templates. Corresponding CBV images were then mapped into group-wise template space using the diffeomorphic vector describing the structural image transformation. Using previously established operational criteria in mice[57] and humans[58,59], the MEC and LEC were defined in group-wise template space (Fig. 7a). A region (MEC/LEC) by side (left/right) interaction was explored in SPSSv21 using mean whole-ROI CBV values in group-wise template space (Fig. 7b). In addition, a mean CBV image was computed from transformed CBV maps in mouse and human group-wise template space. This image map was thresholded above the mean intensity of the MEC and color-coded using Slicer3 (Fig. 7c).

Histological analysis

Mouse brains were harvested after transcardial perfusion with phosphate-buffered saline (PBS) and drop-fixed in 4% paraformaldehyde (wt/vol) overnight, followed by cryoprotection treatment in 30% sucrose (wt/vol) in PBS for 16 h. The whole brain was sectioned throughout on a horizontal plane with a cryostat (35 μm), and collected in individual wells. 64 consecutive brain sections starting from Bregma −4.56 mm[60] were selected and every eighth section ($n = 8$ per set) was combined into one set for each individual antibody. Similarly, 16 consecutive sections starting from the dorsal surface of the brain were collected to represent neocortex, and every eighth section ($n = 2$ per set) was used. Three monoclonal antibodies were used for detection of tau. MC1 (gift from P. Davies; North Shore, LIJ) detects an abnormal conformational epitope of tau that is associated with NFT formation[28]. CP27 is specific for human tau (conformation and phosphorylation status independent, gift from P. Davies). AT8 recognizes tau phosphorylated at S202/205, in mouse and human tau. 6E10 antibody (Covance) was used to detect human APP/βCTF/Aβ.

Free-floating brain sections were first washed with PBS for 10 min, and then treated with 1% H_2O_2 (vol/vol) in PBS for 10 min. The sections were transferred to a microfuge tube that contained 1 ml of primary antibody diluted in PBS containing 0.3% Triton (vol/vol) and 5% normal serum (vol/vol), and incubated at 4 °C overnight on a rotator. After three washes with PBS-T (0.1% Triton X-100), the sections were incubated for 10 min with HRP polymer conjugate (SuperPicTure polymer detection kit, Zymed). Following three washes with PBS-T, immunoreactive material was visualized using DAB as chromagen. The stained sections were mounted on slides and inspected by light microscopy. A semiquantitative analysis of MC1 positive neurons in the entorhinal cortex was performed with 7 EC-APP/Tau and 5 EC-Tau mice from the older mouse group. For each mouse, a total of six MC1 stained horizontal sections starting from Bregma −4.12 mm, spaced at 280 ìm, were included for cell counting (cell bodies only) using the ImageJ software (version 1.44p, US National Institutes of Health).

Gene-expression analysis

The left and the right entorhinal cortices of three 6-month-old wild-type mice were dissected out by following anatomical landmarks[60]. Samples were immediately processed for RNA extraction using the RNeasy Kit from Qiagen according to manufacturer's instructions. Before running the microarrays, RNA quality and integrity was monitored on an Agilent BioAnalyzer. Samples were then run on Affymetrix Genechip Mouse gene 2.0 ST arrays following Affymetrix's standard procedures (n = 3 per cortical hemisphere). Microarray data were analyzed through the use of Ingenuity iReport (Ingenuity Systems, http://www.ingenuity.com).

Acknowledgments

This work was supported by US National Institutes of Health grants AG034618 and AG025161 to S.A.S., AG07232 and AG037212 to R.M., NS074874 to K.E.D., and HL094423 to R.S.

References

1. Braak H, Del Tredici K. Alzheimer's disease: pathogenesis and prevention. Alzheimers Dement. 2012; 8:227–233. [PubMed: 22465174]
2. Gómez-Isla T, et al. Profound loss of layer II entorhinal cortex neurons occurs in very mild Alzheimer's disease. J. Neurosci. 1996; 16:4491–4500. [PubMed: 8699259]
3. Whitwell JL, et al. 3D maps from multiple MRI illustrate changing atrophy patterns as subjects progress from mild cognitive impairment to Alzheimer's disease. Brain. 2007; 130:1777–1786. [PubMed: 17533169]
4. Moreno H, et al. Imaging the abeta-related neurotoxicity of Alzheimer disease. Arch. Neurol. 2007; 64:1467–1477. [PubMed: 17923630]
5. Näslund J, et al. Correlation between elevated levels of amyloid beta-peptide in the brain and cognitive decline. J. Am. Med. Assoc. 2000; 283:1571–1577.
6. Lue LF, et al. Soluble amyloid beta peptide concentration as a predictor of synaptic change in Alzheimer's disease. Am. J. Pathol. 1999; 155:853–862. [PubMed: 10487842]
7. Desikan RS, et al. Amyloid-beta–associated clinical decline occurs only in the presence of elevated P-tau. Arch. Neurol. 2012; 69:709–713. [PubMed: 22529247]
8. Canto CB, Witter MP. Cellular properties of principal neurons in the rat entorhinal cortex. I. The lateral entorhinal cortex. Hippocampus. 2012; 22:1256–1276. [PubMed: 22162008]

9. Canto CB, Witter MP. Cellular properties of principal neurons in the rat entorhinal cortex. II. The medial entorhinal cortex. Hippocampus. 2012; 22:1277–1299. [PubMed: 22161956]
10. Tsao A, Moser MB, Moser EI. Traces of experience in the lateral entorhinal cortex. Curr. Biol. 2013; 23:399–405. [PubMed: 23434282]
11. Canto CB, Wouterlood FG, Witter MP. What does the anatomical organization of the entorhinal cortex tell us? Neural Plast. 2008; 2008:381243. [PubMed: 18769556]
12. Selkoe DJ. Alzheimer's disease is a synaptic failure. Science. 2002; 298:789–791. [PubMed: 12399581]
13. Sperling RA, et al. Toward defining the preclinical stages of Alzheimer's disease: recommendations from the National Institute on Aging-Alzheimer's Association workgroups on diagnostic guidelines for Alzheimer's disease. Alzheimers Dement. 2011; 7:280–292. [PubMed: 21514248]
14. Lin W, Celik A, Paczynski RP. Regional cerebral blood volume: a comparison of the dynamic imaging and the steady state methods. J. Magn. Reson. Imaging. 1999; 9:44–52. [PubMed: 10030649]
15. Raichle ME. Positron emission tomography. Annu. Rev. Neurosci. 1983; 6:249–267. [PubMed: 6340590]
16. Belliveau JW, et al. Functional mapping of the human visual cortex by magnetic resonance imaging. Science. 1991; 254:716–719. [PubMed: 1948051]
17. González RG, et al. Functional MR in the evaluation of dementia: correlation of abnormal dynamic cerebral blood volume measurements with changes in cerebral metabolism on positron emission tomography with fludeoxyglucose F 18. AJNR. Am. J. Neuroradiol. 1995; 16:1763–1770. [PubMed: 8693972]
18. Small SA, Chawla MK, Buonocore M, Rapp PR, Barnes CA. From the cover: imaging correlates of brain function in monkeys and rats isolates a hippocampal subregion differentially vulnerable to aging. Proc. Natl. Acad. Sci. USA. 2004; 101:7181–7186. [PubMed: 15118105]
19. Liu L, et al. Trans-synaptic spread of tau pathology *in vivo*. PLoS ONE. 2012; 7:e31302. [PubMed: 22312444]
20. de Calignon A, et al. Propagation of tau pathology in a model of early Alzheimer's disease. Neuron. 2012; 73:685–697. [PubMed: 22365544]
21. Harris JA, et al. Transsynaptic progression of amyloid-beta-induced neuronal dysfunction within the entorhinal-hippocampal network. Neuron. 2010; 68:428–441. [PubMed: 21040845]
22. Sabuncu MR, Yeo BT, Van Leemput K, Vercauteren T, Golland P. Asymmetric image-template registration. Med. Image Comput. Comput. Assist. Interv. 2009; 12:565–573. [PubMed: 20426033]
23. Brickman AM, Stern Y, Small SA. Hippocampal subregions differentially associate with standardized memory tests. Hippocampus. 2011; 21:923–928. [PubMed: 20824727]
24. Elias MF, et al. The preclinical phase of alzheimer disease: a 22-year prospective study of the Framingham Cohort. Arch. Neurol. 2000; 57:808–813. [PubMed: 10867777]
25. Yasuda M, Mayford MR. CaMKII activation in the entorhinal cortex disrupts previously encoded spatial memory. Neuron. 2006; 50:309–318. [PubMed: 16630840]
26. Moreno H, Hua F, Brown T, Small S. Longitudinal mapping of mouse cerebral blood volume with MRI. NMR Biomed. 2006; 19:535–543. [PubMed: 16552789]
27. Lewis J, et al. Enhanced neurofibrillary degeneration in transgenic mice expressing mutant tau and APP. Science. 2001; 293:1487–1491. [PubMed: 11520987]
28. Jicha GA, Berenfeld B, Davies P. Sequence requirements for formation of conformational variants of tau similar to those found in Alzheimer's disease. J. Neurosci. Res. 1999; 55:713–723. [PubMed: 10220112]
29. Hevner RF, Wong-Riley MT. Entorhinal cortex of the human, monkey, and rat: metabolic map as revealed by cytochrome oxidase. J. Comp. Neurol. 1992; 326:451–469. [PubMed: 1334980]
30. Solodkin A, Van Hoesen GW. Entorhinal cortex modules of the human brain. J. Comp. Neurol. 1996; 365:610–617. [PubMed: 8742306]

31. Kageyama GH, Wong-Riley MT. Histochemical localization of cytochrome oxidase in the hippocampus: correlation with specific neuronal types and afferent pathways. Neuroscience. 1982; 7:2337–2361. [PubMed: 6294558]
32. Schon K, Hasselmo ME, Lopresti ML, Tricarico MD, Stern CE. Persistence of parahippocampal representation in the absence of stimulus input enhances long-term encoding: a functional magnetic resonance imaging study of subsequent memory after a delayed match-to-sample task. J. Neurosci. 2004; 24:11088–11097. [PubMed: 15590925]
33. Olsen RK, et al. Performance-related sustained and anticipatory activity in human medial temporal lobe during delayed match-to-sample. J. Neurosci. 2009; 29:11880–11890. [PubMed: 19776274]
34. Suzuki WA, Amaral DG. Perirhinal and parahippocampal cortices of the macaque monkey: cortical afferents. J. Comp. Neurol. 1994; 350:497–533. [PubMed: 7890828]
35. Young BJ, Otto T, Fox GD, Eichenbaum H. Memory representation within the parahippocampal region. J. Neurosci. 1997; 17:5183–5195. [PubMed: 9185556]
36. Albert MS. The ageing brain: normal and abnormal memory. Phil. Trans. R. Soc. Lond. B. 1997; 352:1703–1709. [PubMed: 9415922]
37. Petersen RC, Smith G, Kokmen E, Ivnik RJ, Tangalos EG. Memory function in normal aging. Neurology. 1992; 42:396–401. [PubMed: 1736173]
38. Stranahan AM, Haberman RP, Gallagher M. Cognitive decline is associated with reduced reelin expression in the entorhinal cortex of aged rats. Cereb. Cortex. 2011; 21:392–400. [PubMed: 20538740]
39. Meguro K, et al. Neocortical and hippocampal glucose hypometabolism following neurotoxic lesions of the entorhinal and perirhinal cortices in the non-human primate as shown by PET. Implications for Alzheimer's disease. Brain. 1999; 122:1519–1531. [PubMed: 10430835]
40. Klunk WE, et al. Imaging brain amyloid in Alzheimer's disease with Pittsburgh Compound-B. Ann. Neurol. 2004; 55:306–319. [PubMed: 14991808]
41. Kageyama GH, Wong-Riley MT. Histochemical localization of cytochrome oxidase in the hippocampus: correlation with specific neuronal types and afferent pathways. Neuroscience. 1982; 7:2337–2361. [PubMed: 6294558]
42. Das U, et al. Activity-induced convergence of APP and BACE-1 in acidic microdomains via an endocytosis-dependent pathway. Neuron. 2013; 79:447–460. [PubMed: 23931995]
43. Ittner LM, et al. Dendritic function of tau mediates amyloid-beta toxicity in Alzheimer's disease mouse models. Cell. 2010; 142:387–397. [PubMed: 20655099]
44. Sapir T, Frotscher M, Levy T, Mandelkow EM, Reiner O. Tau's role in the developing brain: implications for intellectual disability. Hum. Mol. Genet. 2012; 21:1681–1692. [PubMed: 22194194]
45. Brickman AM, et al. Brain morphology in older African Americans, Caribbean Hispanics, and whites from northern Manhattan. Arch. Neurol. 2008; 65:1053–1061. [PubMed: 18695055]
46. Stern Y, et al. Diagnosis of dementia in a heterogeneous population. Development of a neuropsychological paradigm-based diagnosis of dementia and quantified correction for the effects of education. Arch. Neurol. 1992; 49:453–460. [PubMed: 1580806]
47. McKhann G, et al. Clinical diagnosis of Alzheimer's disease: report of the NINCDSADRDA Work Group under the auspices of Department of Health and Human Services Task Force on Alzheimer's Disease. Neurology. 1984; 34:939–944. [PubMed: 6610841]
48. Hughes CP, Berg L, Danziger WL, Coben LA, Martin RL. A new clinical scale for the staging of dementia. Br. J. Psychiatry. 1982; 140:566–572. [PubMed: 7104545]
49. Manly JJ, et al. Frequency and course of mild cognitive impairment in a multiethnic community. Ann. Neurol. 2008; 63:494–506. [PubMed: 18300306]
50. Santacruz K, et al. Tau suppression in a neurodegenerative mouse model improves memory function. Science. 2005; 309:476–481. [PubMed: 16020737]
51. Jankowsky JL, et al. Environmental enrichment mitigates cognitive deficits in a mouse model of Alzheimer's disease. J. Neurosci. 2005; 25:5217–5224. [PubMed: 15917461]
52. Moreno H, Hua F, Brown T, Small S. Longitudinal mapping of mouse cerebral blood volume with MRI. NMR Biomed. 2006; 19:535–543. [PubMed: 16552789]

53. Reuter M, Rosas HD, Fischl B. Highly accurate inverse consistent registration: a robust approach. Neuroimage. 2010; 53:1181–1196. [PubMed: 20637289]

54. Frangi A, Niessen W, Vincken K, Viergever M. Multiscale vessel enhancement filtering. Med. Image Comput. Comput, Assist. Interv. 1998; 1496:130–137.

55. Desikan RS, et al. An automated labeling system for subdividing the human cerebral cortex on MRI scans into gyral based regions of interest. Neuroimage. 2006; 31:968–980. [PubMed: 16530430]

56. Tustison NJ, et al. N4ITK: improved N3 bias correction. IEEE Trans. Med. Imaging. 2010; 29:1310–1320. [PubMed: 20378467]

57. Richards K, et al. Segmentation of the mouse hippocampal formation in magnetic resonance images. Neuroimage. 2011; 58:732–740. [PubMed: 21704710]

58. Zeineh MM, Engel SA, Bookheimer SY. Application of cortical unfolding techniques to functional MRI of the human hippocampal region. Neuroimage. 2000; 11:668–683. [PubMed: 10860795]

59. Mueller SG, et al. Measurement of hippocampal subfields and age-related changes with high resolution MRI at 4T. Neurobiol. Aging. 2007; 28:719–726. [PubMed: 16713659]

60. Paxinos, G.; Franklin, K. The Mouse Brain in Stereotaxic Coordinates. Academic Press; 2001.

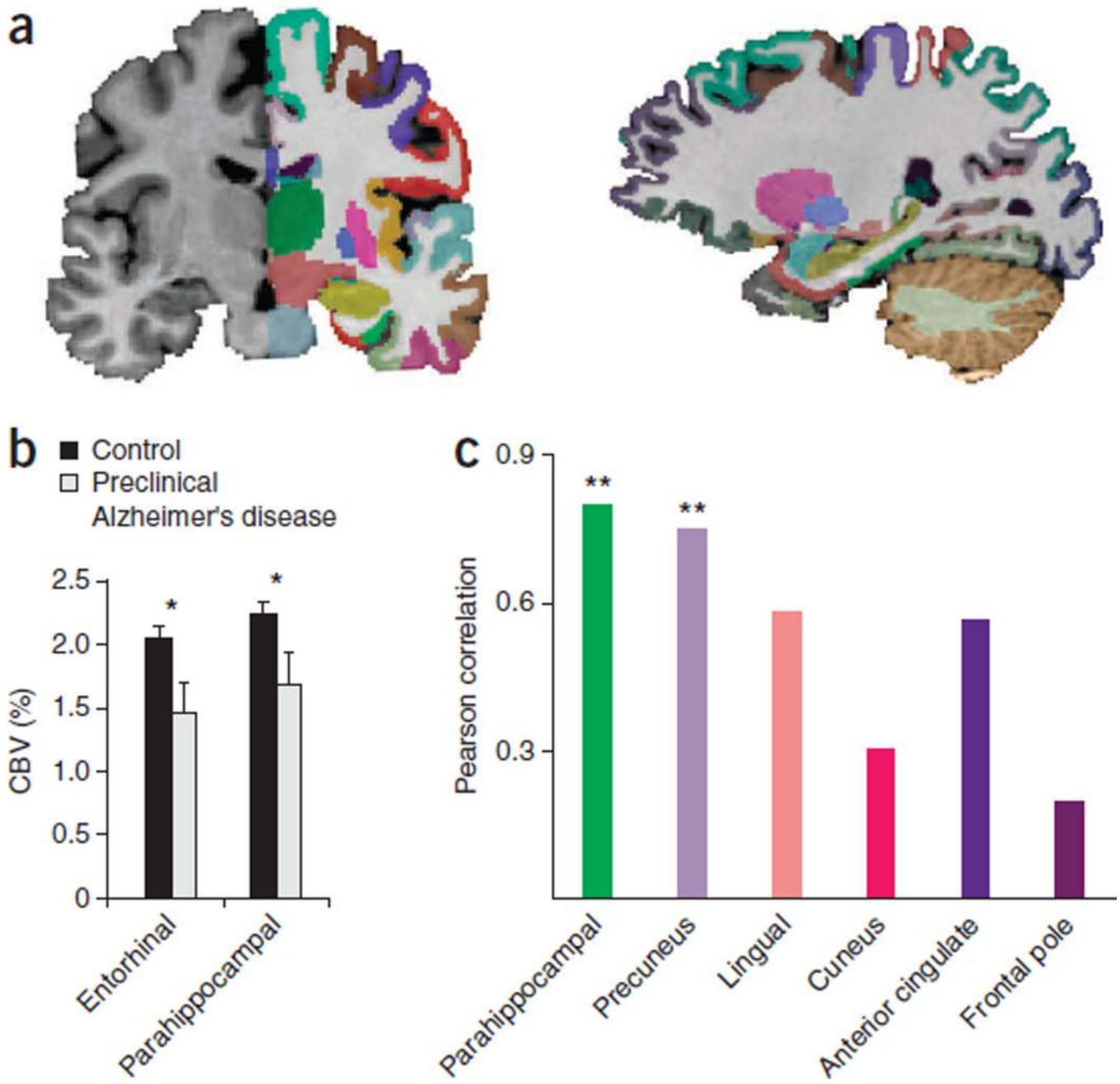

Figure 1.

Whole-brain ROI analysis identified dysfunction in the entorhinal cortex and other cortical regions in preclinical Alzheimer's disease. (**a**) An example of automated whole-brain segmentation of a CBV image. Left, pre-contrast image in a coronal view (for illustration purposes the right brain is shown unsegmented). Right, sagittal view. (**b**) Compared with a control group (light gray bars), the preclinical group (dark gray bars) showed reliable reductions in the percentage of CBV in the entorhinal cortex and parahippocampal gyrus. *$P < 0.05$. Error bars represent s.e.m. (**c**) Among brain regions affected in preclinical Alzheimer's disease, only the parahippocampal gyrus and the precuneus cortex were

significantly correlated with entorhinal cortex dysfunction by a correlational analysis (**Pearson correlation coefficient >0.7).

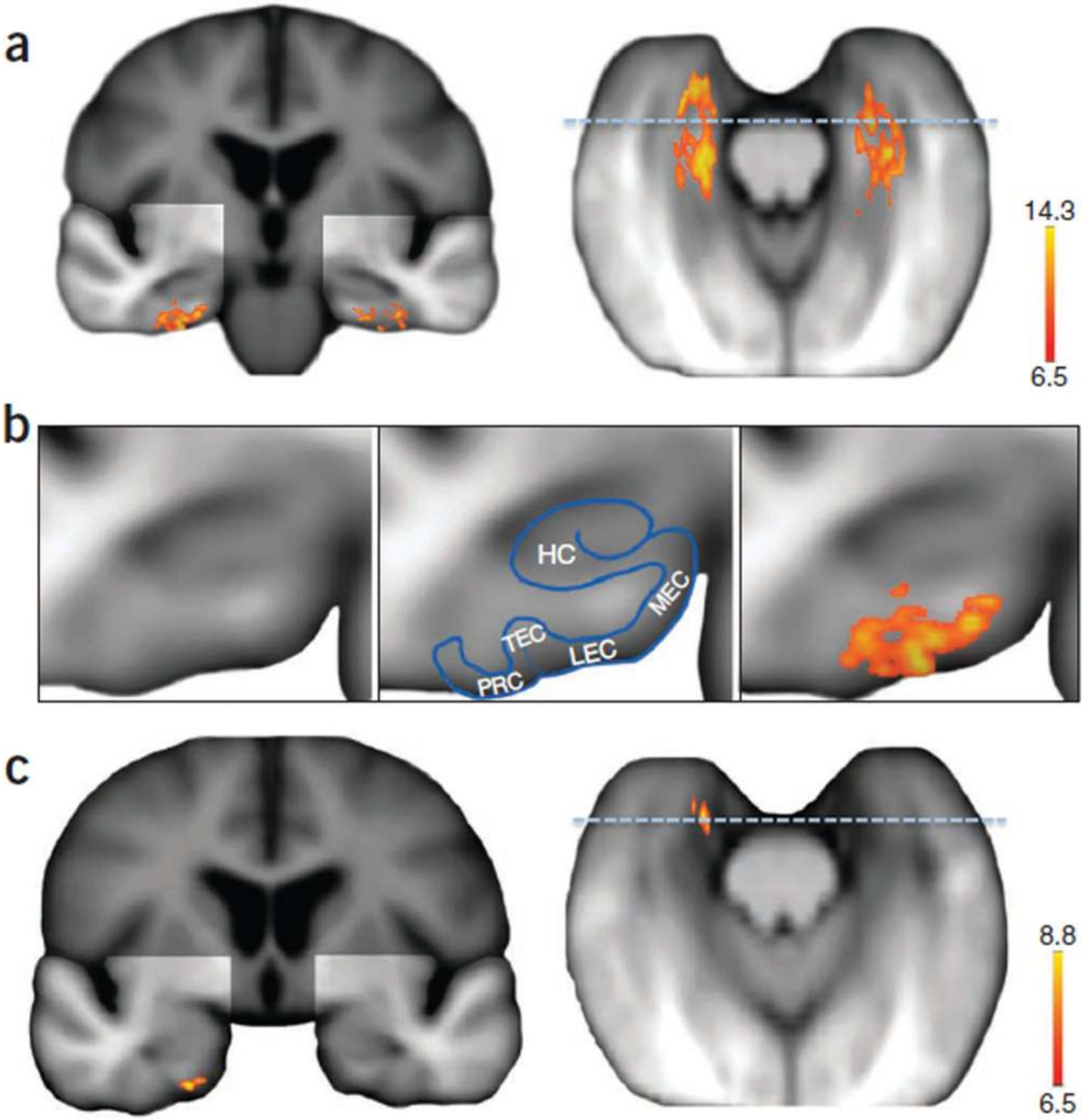

Figure 2.

Voxel-based analysis pinpoints dysfunction in preclinical Alzheimer's disease to the LEC. (**a**) A voxel-based analysis was performed in the temporal lobes (indicated by highlighted areas at left) and the voxels that showed significantly lower CBV in the preclinical are indicated in color in a coronal view (left) and an axial view (right). (**b**) A higher magnification of the coronal view showing the anatomy of the medial temporal (left and middle). Right, LEC and PRC were the regions with reliable CBV reductions in the preclinical compared to the control group. TEC, transentorhinal cortex; HC, hippocampus

proper. (**c**) An analysis of the control group pinpointed the right LEC as a region in which CBV was correlated with performance on a delayed retention task. Statistics are represented as heat maps of *t* values corresponding to $P < 0.05$, corrected for multiple comparisons using the FWE approach.

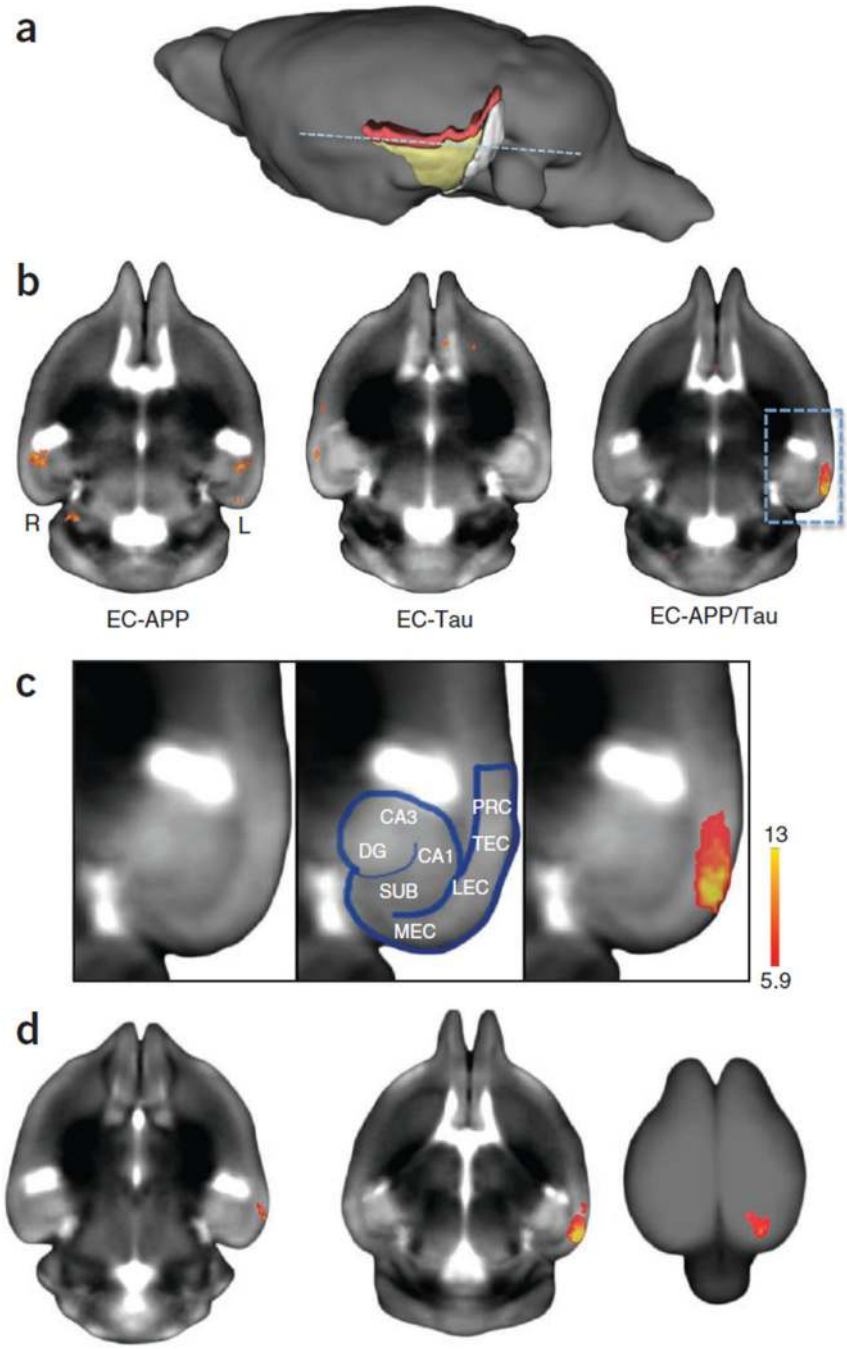

Figure 3.

The LEC is affected by tau and APP coexpression and leads to cortical dysfunction. (**a**) A volume rendering of the mouse brain, mapping the anatomical locations of the LEC (yellow), MEC (white) and PRC (red). (**b**) Voxel-based analyses revealed that, compared with controls, EC-APP mice had CBV reductions in the MEC and the CA1 (left), EC-Tau mice showed little differences in CBV (middle), and EC-APP/Tau mice had reliable CBV reductions [in the left LEC and PRC (right). All images are axial slices whose location is illustrated in the volume rendering shown in **a**. (**c**) A higher magnification of the slice (as

illustrated in the stippled box in the right panel of **b**) shows the anatomy of the medial temporal region (left and middle; SUB, subiculum; DG, dentate gyrus), and shows that the LEC and the PRC were the regions with reliable CBV reductions in the EC-APP/Tau group (right). (**d**) More dorsal slices of the EC-APP/Tau group showing additional areas of reduced CBV in the PRC (left and middle) and reduced CBV in PPC (right).

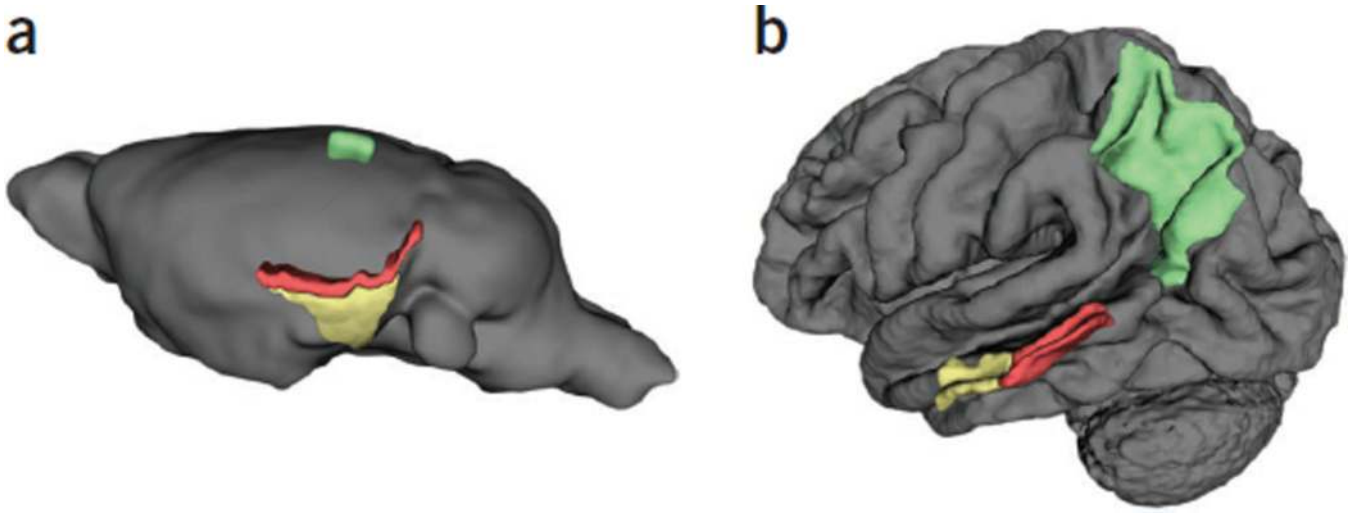

Figure 4.

Patterns of cortical spread in mouse models overlap with patterns observed in preclinical Alzheimer's disease. (**a**) As illustrated by volume rendering, the brain regions affected in the EC-APP/Tau mice are the LEC (yellow), PRC (red) and the PPC (green). (**b**) As illustrated by volume rendering, among the regions affected in the human preclinical group, dysfunction in the entorhinal cortex (yellow) was reliably correlated with CBV in the parahippocampal gyrus (red) and precuneus (green).

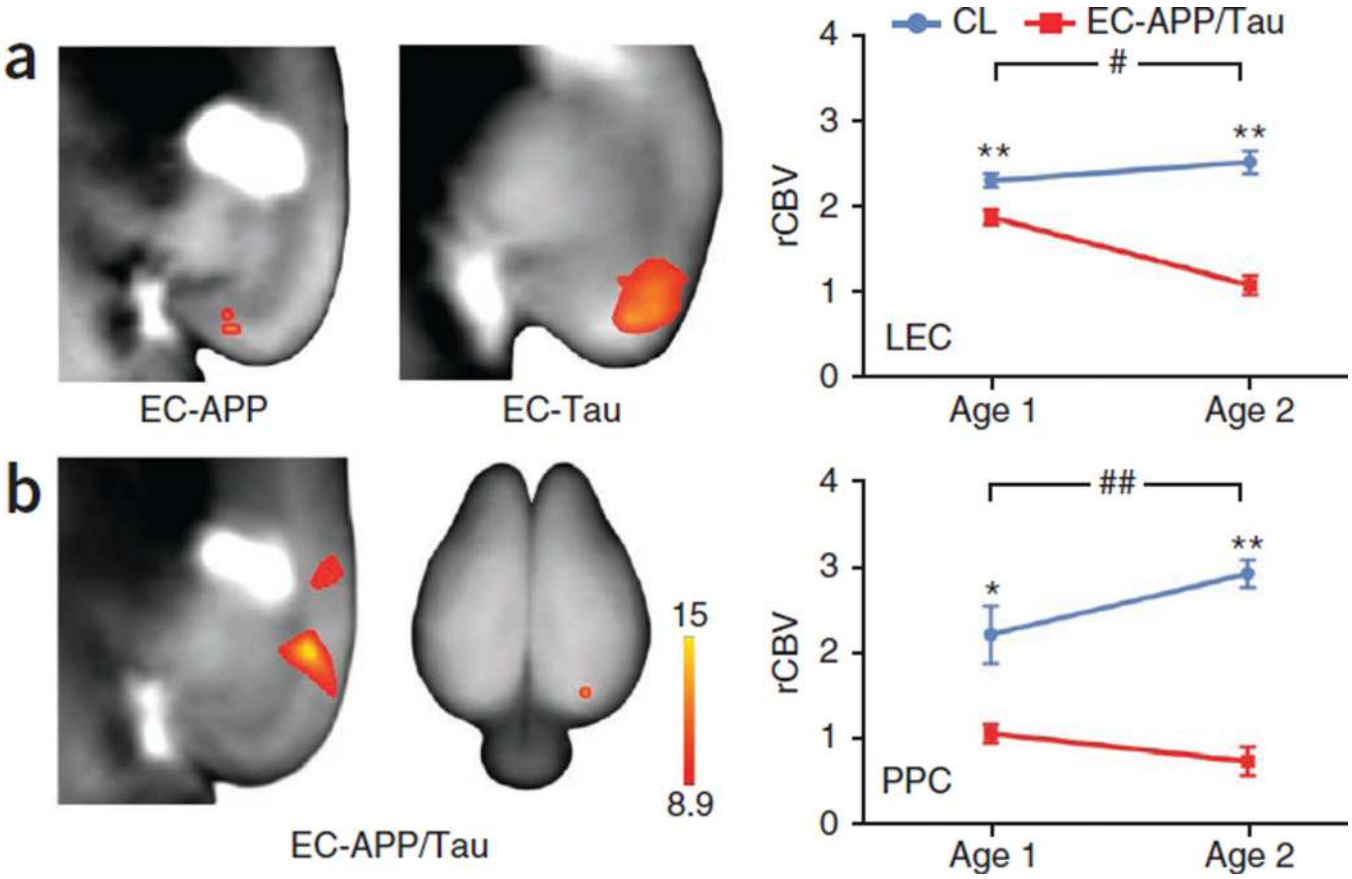

Figure 5.

APP expression acts to potentiate and accelerate tau toxicity in the LEC. (**a**) Mapping group × age interactions revealed that age-dependent worsening of relative CBV (rCBV) was increased in the MEC of EC-APP mice compared with their controls (left) and increased in the LEC of EC-Tau mice compared with their controls (right). (**b**) Mapping a group × age interaction revealed age-dependent worsening of CBV in the LEC and PRC (left), and the PPC (right), of EC-APP/Tau mice compared with EC-APP and EC-Tau mice. Line graph illustrations of the group × age interactions in the LEC (upper graph) and the PPC (lower graph) of EC-APP/Tau (red) mice compared with EC-APP and EC-Tau mice (blue). $^{*}P < 0.05$, $^{**}P < 0.001$; $^{\#}F_{1,83} = 14.346$, $P = 0.0003$; $^{\#\#}F_{1,83} = 4.829$, $P = 0.031$. Data are presented as mean ± s.e.m.

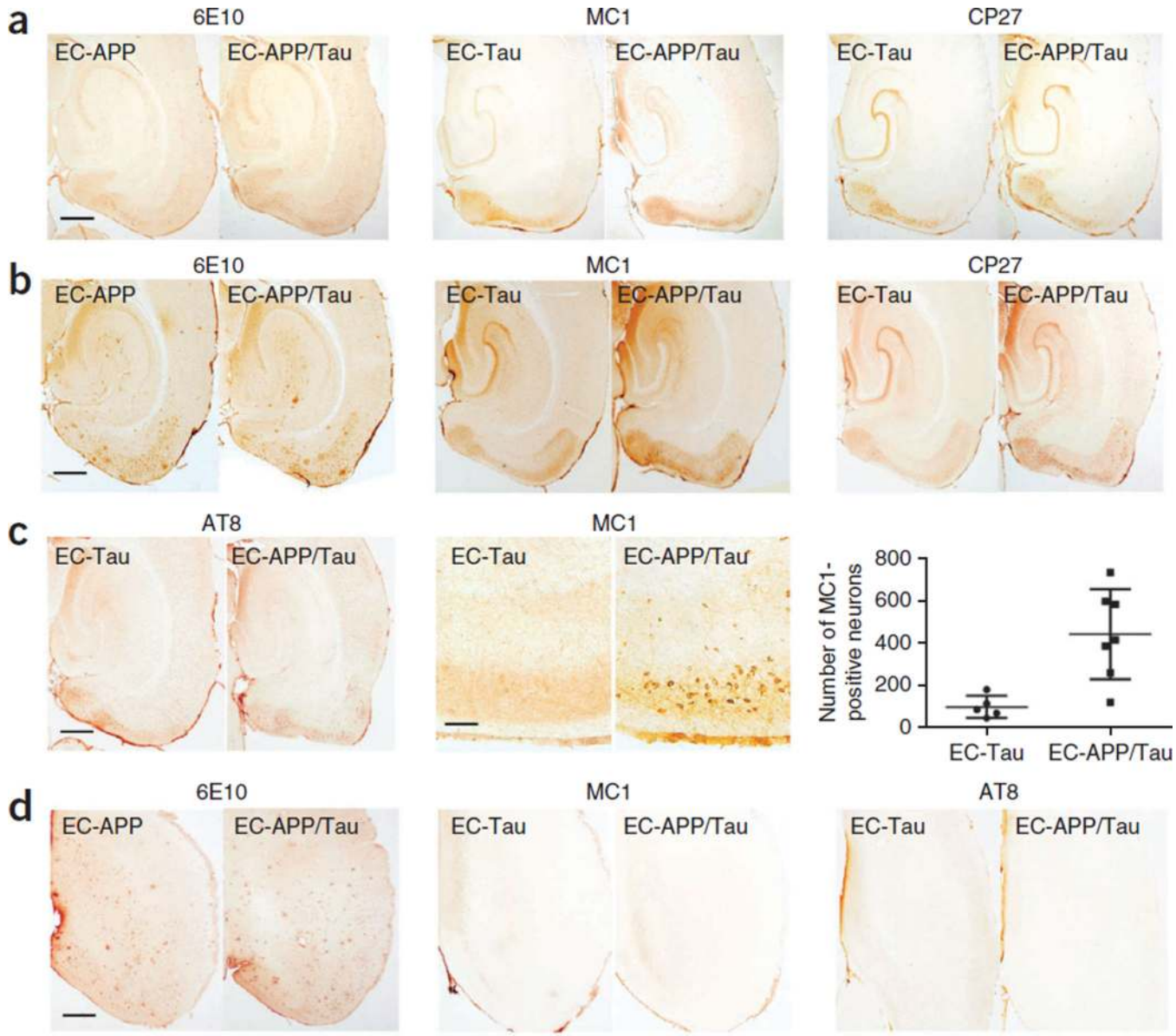

Figure 6.

Mapping histological markers of tau and APP in mouse models. (**a**) Histology analysis in the MTL of APP/Aβ with 6E10 antibody in young EC-APP and EC-APP/Tau mice (left), abnormally conformed human tau with MC1 antibody in young EC-Tau and EC-APP/Tau mice (middle), and total human tau with CP27 antibody in young EC-Tau and EC-APP/Tau (right). Scale bar represents 500 μm.

(**b**) Histology analysis in the MTL of APP/Aβ with 6E10 antibody in old EC-APP and EC-APP/Tau mice (left), conformation changes in tau with MC1 antibody in old EC-Tau and EC-APP/Tau mice (middle), and total human tau with CP27 antibody in old EC-Tau and ECAPP/Tau mice (right). Scale bar represents 500 μm. (**c**) Histology analysis in the MTL of phospho-tau with AT8 antibody in old EC-Tau and EC-APP/Tau mice (left). In older EC-APP/Tau mice, MC1 immunohistochemistry (20×) revealed the occurrence of redistribution

of tau from axons into the somatodendritic compartments compared with EC-Tau mice (middle). A semiquantitative analysis revealed a significant increase in MC1-positive neurons in the entorhinal cortex in the EC-APP/Tau mice (440.1 ± 79.60, $n = 7$), mainly in the MEC, compared with the EC-Tau mice (99.80 ± 22.92, $n = 5$; t-test, $P = 0.006$; right). Data are presented as mean ± s.e.m. Scale bars represent 500 μm (left) and 100 μm (middle). (**d**) Histology analysis in the parietal lobe of APP/Aβ with 6E10 antibody in old EC-APP and EC-APP/Tau mice (left), conformation changes in tau with MC1 antibody in old EC-Tau and EC-APP/Tau mice (middle), and phospho-tau with AT8 antibody in old EC-Tau and EC-APP/Tau mice (right). Scale bar represents 500 μm.

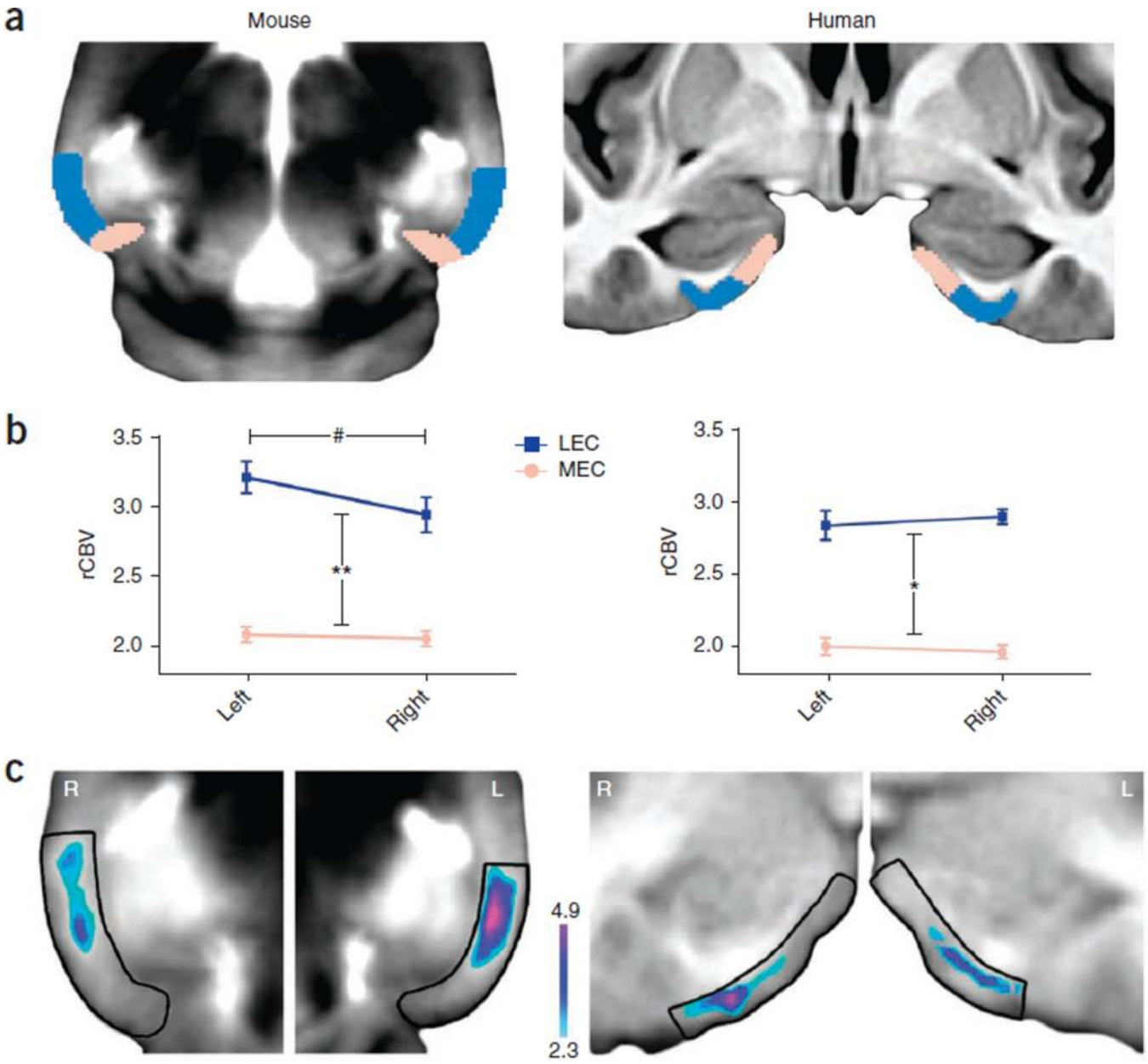

Figure 7.

The LEC shows evidence of high metabolism in young unaffected individuals. (**a**) The entorhinal cortex was segmented into the MEC (pink) and the LEC (blue) in template brains of young wild-type mice (left) and young healthy human subjects (right). (**b**) In young wild-type mice (left), the LEC (blue) was found to have higher CBV values than the MEC (pink) (**$F_{1,34}$ = 475.176, P < 0.001), and the left LEC was found to have higher CBV values than the right LEC ($^{\#}F_{1,34}$ = 6.680, P = 0.01). In young healthy human subjects (right), the LEC (blue) was found to have higher CBV values than the MEC (pink) (*$F_{1,34}$ = 706.199, P < 0.001). Data are presented as mean ± s.e.m. (**c**) Thresholded mean CBV maps in young wild-type mice (left) revealed that the CBV was higher in the LEC than the MEC, with the

left LEC showing the highest CBV. Mean CBV maps in young healthy human subjects (right) revealed that the LEC had a higher CBV than the MEC.

Table 1

Baseline and change in cognitive performance in the group that progressed to dementia and the group that did not progress

	Non-progressors	Progressors	Statistics
Memory baseline	39.3	35.1	$F_{1,90} = 1.8$, $P = 0.18$
Memory change	−1.9	−11.8	$F_{1,90} = 8.0$, $P = 0.006$
Language baseline	34.8	32.7	$F_{1,90} = 0.2$, $P = 0.62$
Language change	−2.0	−7.8	$F_{1,90} = 4.8$, $P = 0.03$
Visuospatial baseline	2.8	2.3	$F_{1,90} = 2.7$, $P = 0.11$
Visuospatial change	−0.7	−7.0	$F_{1,90} = 2.5$, $P = 0.12$
Abstract reasoning baseline	15.5	11.0	$F_{1,90} = 8.4$, $P = 0.005$
Abstract reasoning change	−0.1	−3.8	$F_{1,90} = 3.8$, $P = 0.056$